Mechanism for epitaxial breakdown during low-temperature Ge(001) molecular beam epitaxy

K. A. Bratland, Y. L. Foo, J. A. N. T. Soares, T. Spila, P. Desjardins,* and J. E. Greene

Materials Science Department and the Frederick Seitz Materials Research Laboratory, University of Illinois,
104 South Goodwin Avenue, Urbana, Illinois 61801

A combination of *in situ* and post-deposition experiments were designed to probe surface roughening pathways leading to epitaxial breakdown during low-temperature ($T_s = 95-190$ °C) growth of Ge(001) by molecular beam epitaxy (MBE). We demonstrate that epitaxial breakdown in these experiments is not controlled by background hydrogen adsorption or gradual defect accumulation as previously suggested, but is a growth-mode transition driven by kinetic surface roughening. Ge(001) layers grown at $T_s \gtrsim 170$ °C remain fully epitaxial to thicknesses $h > 1.6$ μm, while deposition at $T_s < 170$ °C leads to a locally abrupt transition from epitaxial to amorphous growth at critical film thicknesses $h_2(T_s)$. Surface morphology during low-temperature Ge(001) MBE evolves via the formation of a periodic array of self-organized round growth mounds which, for deposition at $T_s > 115$ °C, transform to a pyramidal shape with square bases having edges aligned along $\langle 100 \rangle$ directions. Surface widths w and in-plane coherence lengths d increase monotonically with film thickness h at a temperature-dependent rate. As $h \rightarrow h_1(T_s)$, defined as the onset of epitaxial breakdown, deep cusps bounded by {111} facets form at the base of interisland trenches and we show that epitaxial breakdown is initiated on these facets as the surface roughness reaches a critical T_s-independent aspect ratio $w/d \simeq 0.02$. $h_{1(2)}(T_s)$ and $h_2(T_s)$ follow relationships $h_{1(2)} \propto \exp(-E_{1(2)}/kT_s)$, where E_1 is 0.61 eV and $E_2 = 0.48$ eV. E_1 is approximately equal to the Ge adatom diffusion barrier on Ge(001) while $(E_1 - E_2) = 0.13$ eV is the free energy difference between crystalline and amorphous Ge. We summarize our results in a microstructural phase map vs T_s and h, and propose an atomistic growth model to explain the epitaxial to amorphous phase transition.

I. INTRODUCTION

The development of a detailed atomic-level understanding of epitaxial growth at low temperatures (LT) is of interest for both scientific and technological reasons. Thin film applications require ever lower growth temperatures in order to, for example, obtain abrupt interfaces in multilayer devices, minimize alloy and dopant interlayer diffusion, reduce dopant surface segregation, and inhibit phase transitions in metastable materials. However, low growth temperatures lead to kinetic roughening[1-9] due to correspondingly low adatom mobilities and the presence of Ehrlich barriers,[10] and/or deep traps, at descending step edges. The latter results in a divergence in adatom currents giving rise to increased island nucleation on upper terraces and the formation of a regular array of growth mounds whose surface width w and in-plane coherence length d increase with increasing film thickness.[4,7] The surface roughness continues to increase with film thickness until the growth front breaks down in an irreversible transition to amorphous layer deposition.[11-13]

The first observation that a limited epitaxial thickness can be achieved at T_s far below values believed to be the "minimum" possible epitaxial temperature was reported in 1966 by Jona,[14] and later confirmed by de Jong,[15] using low-energy electron diffraction to show that a few monolayers of epitaxial Si could be deposited on Si(001)2×1 at room temperature. In 1986, Aarts *et al.*[16] observed reflection high-energy electron diffraction (RHEED) oscillations at 25 °C during growth of homoepitaxial Ge(001)2×1 layers, but no structural analyses were provided. These initial reports led to a renewed interest in the fundamental limits of low-

temperature epitaxial growth and more detailed investigations of homoepitaxial Si(001),[17-20] Si(111),[19] Ge(001),[4,7,13] GaAs(001),[19,21] and heteroepitaxial Ge/Si(001) (Ref. 22) and $Ge_{1-x}Sn_x$/Ge(001) (Refs. 23 and 24) by low-temperature (LT) molecular beam epitaxy (MBE). All results showed that there is a critical, temperature-dependent, epitaxial thickness, rather than a unique epitaxial temperature, at which a transition from epitaxial to amorphous growth is observed. This crystalline/amorphous phase transformation is typically preceded by the growth of an intermediate sublayer with a high defect density.[11,13,25]

The epitaxial thickness has been defined in a variety of ways in prior reports. Here, we define two critical thicknesses based upon direct experimental observation. $h_1(T_s)$ is the film thickness at which bulk structural defects are first observed by RHEED and cross-sectional transmission electron microscopy (XTEM), while $h_2(T_s)$ corresponds to the thickness at which the entire layer has transformed from epitaxial to amorphous. While these definitions, as those used in previous papers, depend upon experimental resolution, they are self-consistent and reproducible as a function of T_s.

Despite numerous investigations of LT epitaxy, a complete understanding of the atomic mechanisms responsible for epitaxial breakdown has not emerged. Several models, including defect accumulation,[25] continuous breakdown,[17,25] hydrogen-induced breakdown,[25-30] and kinetic roughening[4,6-8,11-13,24,25] have been suggested to explain the observed epitaxial-to-amorphous transition. Defect accumulation and continuous breakdown models involve, in their simplest form, a continuous temperature-dependent increase in the concentration of lattice disorder. It has also been pro-

posed that adsorbed hydrogen from the residual background gas leads to epitaxial breakdown as H terminates dangling bonds, thereby altering the surface reconstruction template and hindering adatom migration.[25–30] Intentional H_2 dosing at $\simeq 2 \times 10^{-2}$ ML s^{-1} ($P_{H_2} = 2 \times 10^{-6}$ Torr) during MBE Si(001) growth at $T_s = 310$ and 200 °C with $R = 1.0$ Å s^{-1} decreased the epitaxial thickness from $\simeq 1000$ to 200 Å and from $\simeq 300$ to 20 Å, respectively.[25–28] Finally, there is evidence indicating that kinetic surface roughening itself plays an important role in controlling epitaxial breakdown.[4,6–8,13,24] During LT Si(001) and Ge(001) homoepitaxial growth, the surface roughness has been shown to increase rapidly near $h = h_1(T_s)$.[4,6,8,13,25]

In this paper, we present results on the solid-source MBE growth of homoepitaxial Ge(001) over the temperature range $T_s = 95$–190 °C at a deposition rate $R = 0.5$ Å s^{-1}. Surface structural transitions during growth were monitored using *in situ* RHEED in combination with post-deposition atomic force microscopy (AFM), XTEM, and high-resolution (HR) XTEM. All films grown at $T_s \gtrsim 170$ °C remain epitaxial to layer thicknesses in excess of 1.6 μm. Ge(001) growth at $T_s < 170$ °C is characterized by the presence of three distinct sublayers. For $h < h_1(T_s)$, the bulk Ge(001) layers appear structurally perfect while surface morphology evolves via the formation of a periodic array of growth mounds preferentially bounded along $\langle 100 \rangle$ directions. Surface widths w and in-plane coherence lengths d increase monotonically with film thickness. As $h \to h_1$, deep cusps bounded by {111} facets form at the base of interisland trenches as the surface roughness reaches a critical aspect ratio $w/d \simeq 0.02$, which is independent of T_s. Continued deposition to thicknesses $h_1 < h < h_2$ results in the formation of bulk structural defects including 111 twins and stacking faults. The transition from epitaxial (although highly defective) to amorphous growth is complete at $h_2(T_s)$. The epitaxial-to-amorphous transition is locally atomically abrupt, but the interface is quite rough globally. Both h_1 and h_2 increase with T_s following the relationship $h_{1(2)} \propto \exp(-E_{1(2)}/kT_s)$ with activation energies E_1 and E_2 of 0.61 ± 0.05 and 0.48 ± 0.05 eV, respectively.

We demonstrate conclusively that low-temperature epitaxial breakdown in our experiments is not controlled by the H_2 background pressure, even at H_2 partial pressures P_{H_2} up to 10^{-7} Torr. Rather, we establish low-temperature epitaxial breakdown as a growth mode transition and show that there is a direct correlation between epitaxial breakdown and kinetic roughening. The results are summarized in the form of a microstructural phase map plotted versus T_s and h. The crystalline/amorphous phase transition is discussed in terms of an atomistic growth model in which deposition on {111} faceted cusps leads to double-positioning and other symmetry-breaking defects resulting in a loss of long-range order.

II. EXPERIMENTAL PROCEDURE

All Ge(001) layers were grown in a load-locked multi-chamber MBE system with a base pressure of 5×10^{-11} Torr. A pyrolytic BN effusion cell was used to evaporate

99.9999% pure Ge chunks with resistivity $\geqslant 40$ Ω cm. The effusion cell temperature was continuously monitored and maintained constant to within ± 1 °C during film growth using proportional-band feedback control. The effect of residual hydrogen on LT epitaxy was investigated by backfilling the growth chamber with 99.9999% pure H_2 to partial pressures of up to 1×10^{-7} Torr during growth.

Film surface structural transitions were monitored *in situ* by RHEED, utilizing a 20 kV primary electron beam which intersected the sample at an incidence angle of $\simeq 2°$. A Tektronix C-5C oscilloscope camera was used to acquire the RHEED images. The combination of a quartz-crystal microbalance and an electron-impact emission sensor, calibrated using Ge film thicknesses measured by microstylus profilometry, provided continuous *in situ* measurements of film growth rates R.

The substrates were polished 1.5×2.5 cm^2 Ge(001) plates cleaved from 0.5-mm-thick n-type wafers with a miscut of 0.1° in the [110] direction and room temperature resistivities of 1–20 Ω cm ($n = 1 \times 10^{15}$–6×10^{13} cm^{-3}). Substrate cleaning consisted of rinsing in deionized water to remove the native oxide followed by repeated cycles of oxidation, via a UV-ozone process,[31] and oxide dissolution with the final step being the formation of a clean protective UV-ozone oxide cap layer. The wafers are then bonded to a Mo substrate holder with In and immediately inserted into the UHV system where they are degassed at 250 °C for 45 min and the oxide is desorbed at $T_s \geqslant 450$ °C. This procedure provides clean Ge surfaces with sharp 2×1 RHEED patterns and no impurities detectable by *in situ* Auger or x-ray photoelectron spectroscopies. 600-Å-thick Ge buffer layers deposited at 400 °C with $R = 0.5$ Å s^{-1} also exhibited 2×1 RHEED patterns with sharp Kikuchi lines indicating atomically smooth surfaces. Average terrace lengths are $\geqslant 800$ Å as measured by scanning tunneling microscopy (STM).[4,7]

Homoepitaxial Ge(001) layers were grown over the temperature range $T_s = 95$–190 °C with R maintained constant at 0.5 Å s^{-1}. Film growth temperatures were controlled based on substrate heater power which was calibrated using thermocouples bonded to dummy substrates. The system was recalibrated periodically to correct for thermal drift and to determine reproducibility. Sample temperatures during growth were maintained to within ± 5 °C and absolute values are accurate to within ± 10 °C.

The microstructure and crystalline quality of the layers were investigated using XTEM and HR-XTEM in Philips CM12 and Hitachi H-9000 microscopes operated at 120 and 300 kV, respectively. Specimens were prepared by gluing two samples film-to-film and then cutting a vertical section which was thinned to $\simeq 20$ μm by mechanical grinding. Final thinning to electron transparency was accomplished by Ar$^+$ ion milling in a liquid-N_2-cooled stage with the incident beam angle and energy progressively reduced from 10° to 8° and 5 to 1.5 kV in order to obtain samples with relatively even thickness distributions.

A Digital Instruments Multimode AFM, operating in tapping mode, was used to investigate surface morphological evolution in as-deposited Ge(001) layers. The measurements were carried out in air using oxide-sharpened Si tips having
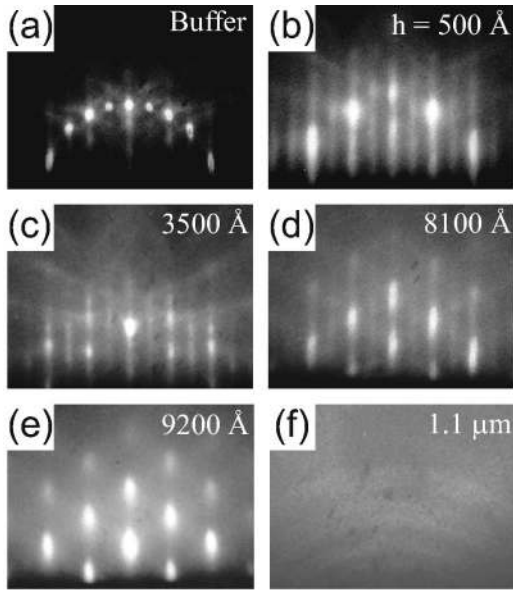
FIG. 1. RHEED patterns obtained along the [110] azimuth (a) following MBE growth of a 600-Å-thick Ge buffer layer on Ge(001) at 400 °C and during growth of a homoepitaxial Ge(001) at $T_s = 155$ °C with $R = 0.5$ Å s^{-1} to thicknesses (b) $h = 500$, (c) 3500, (d) 8100, (e) 9200, and (f) >11 000 Å.

average tip radii of 50–100 Å. Images were linearly planarized to remove sample tilting effects. The surface roughness was quantified using the height-height correlation function $H(\rho) = \langle h_i h_j \rangle$ and the height-difference correlation function $G(\rho) = \langle |h_i - h_j|^2 \rangle$, where h is the height at positions i and j separated by a distance ρ and the brackets correspond to averages over the measured surface. The mean interisland separation d is extracted from the position of the first local maximum in $H(\rho)$. The correlation functions are related to the surface width w, which is equivalent to the root mean square (r.m.s.) roughness, through the relationship $2w^2 = G(\rho) + 2H(\rho)$. $[G(\rho \to \infty)]^{1/2}$ is directly proportional to w in these experiments since $H(\rho \to \infty) \to 0$, consistent with STM results showing that the high-temperature Ge buffer layers are extremely flat.[4,7] Values of w and d were obtained by averaging over at least three different 1×1 μm regions of each sample. Two-dimensional slope histograms were constructed from the vector normals to the surface at all points in the AFM images and are plotted with increasing surface angle from the center of the image.

III. EXPERIMENTAL RESULTS

Low-temperature growth of Ge(001) results in kinetic roughening and limited epitaxial thicknesses. We used RHEED, XTEM, and AFM to follow surface morphological evolution leading to epitaxial breakdown and to determine h_1 and h_2 as a function of film growth temperature T_s. Typical RHEED results obtained along the [110] azimuth are shown in Fig. 1 for Ge(001) layers deposited at $T_s = 155$ °C. Patterns from buffer layers [e.g., Fig. 1(a)] consist of sharp 2×1 spots, with nearly equi-intense fundamental and half-order features, characteristic of a very flat surface. During LT-MBE

growth, the diffraction features become streaky, the half-order intensities gradually decrease, diffuse scattering increases, and the fundamental diffraction rods broaden. An example is shown in Fig. 1(b), corresponding to a Ge(001) layer with $h \simeq 500$ Å. The observed changes in the RHEED patterns as a function of h are indicative of a continuous decrease in the average size of 2×1 reconstructed terraces, increasing step densities, and surface roughening.[32,33] With further deposition, vertical intensity modulations become visible along the length of the fundamental diffraction rods signaling island formation in a multilayer two-dimensional (2D) growth mode[34] [see, for example, Fig. 1(c) corresponding to $h = 3500$ Å]. The modulations continue to increase in intensity with increasing layer thickness. Low-intensity streaks near, or along, $\langle 111 \rangle$ directions appear at $h \simeq 8100$ Å [Fig. 1(d)] signifying the development, as confirmed by HR-XTEM (see below), of {111} facets.

As the surface continues to roughen, the half order streaks disappear, diffuse scattering increases, and the pattern gradually transforms to being three dimensional (3D) as shown in Fig. 1(e), $h = 9200$ Å. The bulk diffraction spots are broad and elongated along the [001] growth direction. The broadening is inversely related to the mean interisland separation while the elongation along [001] indicates that the average island height is less than the lateral size. Continued deposition gives rise to a decrease in the elongation of the bulk diffraction spots as the islands grow faster in the vertical than the lateral direction. The diffracted beams are also increasingly triangular-shaped as the low-intensity $\langle 111 \rangle$ streaks become more distinct. With further deposition, the bulk RHEED diffraction spots gradually decrease in intensity, due to the formation of the amorphous phase, and then completely disappear [see, for example, Fig. 1(f)].

The surface roughening process follows the same reaction path in all layers grown at $T_s \lesssim 170$ °C, but occurs more rapidly at lower T_s. $h_1(T_s)$ is determined from RHEED observations as the film thickness at which $\langle 111 \rangle$ streaks are first observed and $h_2(T_s)$ is defined as the thickness at which the bulk diffraction spots completely disappear.

The microstructural evolution of LT-MBE Ge(001) layers was followed as a function of h and T_s using XTEM. HR-XTEM images (not shown) reveal that for all samples, 111 lattice fringes are continuous through the film/substrate interface. Typical bright-field [110] zone-axis XTEM and HR-XTEM micrographs from Ge(001) films grown at $T_s = 95$ and 135 °C, illustrating the sequence of structural changes observed in all films, are shown in Fig. 2. Ge(001) layers deposited at $T_s \lesssim 170$ °C exhibit three distinct regimes. The first is a defect-free sublayer, as judged by both XTEM and HR-XTEM, extending to h_1 as shown in Figs. 2(a) ($h = 2100$ Å and $T_s = 95$ °C) and 2(c) ($h = 6750$ Å and $T_s = 135$ °C). $h_1(T_s)$ determined from XTEM images is defined as the layer thickness at which bulk structural defects are first observed. Values were obtained from examination of several micrographs, corresponding to >2 μm of interface, for each sample investigated. h_1 increases monotonically with T_s, ranging from $\simeq 650$ Å at 95 °C to 2700 Å at 135 °C.

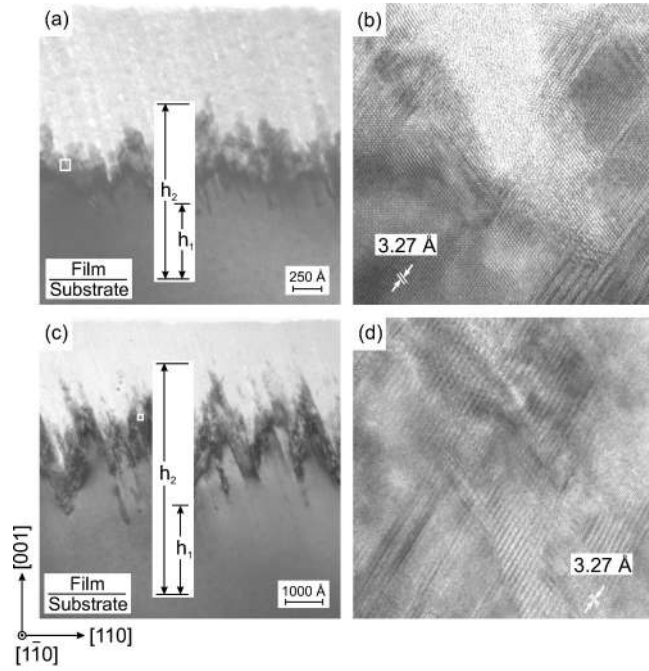Deposition beyond h_1 leads to the formation of a defective, but still epitaxial, region containing 111 stacking faults,

FIG. 2. [110] bright-field zone-axis XTEM micrographs of Ge(001) layers grown by LT-MBE at T_s with $R = 0.5$ Å s^{-1} to thicknesses h. (a) $T_s = 95$ °C, $h = 2100$ Å and (c) $T_s = 135$ °C, $h = 6750$ Å. (b) and (d) are HR-XTEM images of the regions outlined by the small open white squares in (a) and (c), respectively.
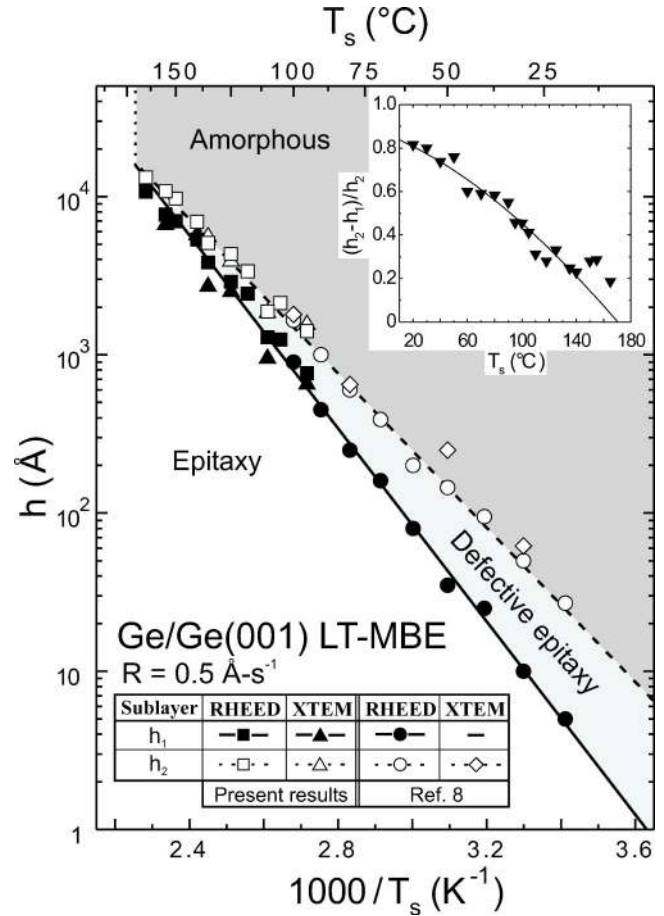

FIG. 3. Microstructural phase diagram of Ge(001) layers grown by LT-MBE as a function of T_s with $R = 0.5$ Å s^{-1}. h_1 is the thickness of the defect-free region and h_2 is the total (defect-free plus defective) maximum epitaxial thickness. Data over the range $T_s = 20–100$ °C is from Ref. 8.

initiated by double-positioning defects on {111} facet planes and microtwins. Examples are shown in Figs. 2(b) and 2(d) which are HR-XTEM images of the regions outlined by the small open white squares in Figs. 2(a) and 2(c), respectively. The growth mode transforms to an amorphous overlayer with a columnar microstructure at a total thickness h_2 [also labeled in Figs. 2(a) and 2(c)]. We define $h_2(T_s)$ in XTEM micrographs as the thickness at which the entire layer has transformed from epitaxial to amorphous. h_2 increases from $\simeq 1550$ Å at 95 °C to 5600 Å at 135 °C. The interface between the defective epitaxial region and the amorphous phase is, although locally atomically abrupt, globally rough and triangular shaped (in a two-dimensional projection), with {111} facets. Although the interface shape remains self-similar, the amplitude and period both increase with T_s. HR-XTEM results also show that the number density of 111 stacking faults and microtwins increases with T_s [compare, for example, Figs. 2(b) and 2(d)].

LT-MBE Ge(001) growth to thicknesses $h > h_1$ at $T_s = 95–170$ °C leads, in addition to stacking faults, to the formation of columnar structures with open boundaries tilted toward the direction of the incident flux, $\simeq 20°$ from the substrate normal. This is also shown in Figs. 2(a) and 2(c). The voided boundaries, whose widths increase with T_s, originate at the onset of the defective epitaxial sublayer and extend to the crystalline/amorphous interface where they evolve into the open intercolumnar boundaries on the amorphous side.

RHEED and XTEM results for Ge(001) LT-MBE are summarized in Fig. 3 as a microstructural phase map plotted as h_1 and h_2 vs T_s (95–190 °C). Data from previous experiments carried out in the same growth system at T_s

$= 20–100$ °C (Ref. 8) are also included in Fig. 3. The total set of results, which overlap at $T_s = 95–100$ °C, are remarkably consistent over the entire temperature range. h_1 and h_2 increase exponentially with T_s and are well fit by the following expressions:

$$h_1 \propto \exp\left[\frac{-E_1}{kT_s}\right],$$

$$h_2 \propto \exp\left[\frac{-E_2}{kT_s}\right], \tag{1}$$

where E_1 and E_2 are 0.61 ± 0.05 and 0.48 ± 0.05 eV, respectively. E_1 is approximately equal to the activation energy for Ge adatom diffusion along dimer rows on the Ge(001)2×1 reconstructed surface.[7] The $h_1(T_s)$ and $h_2(T_s)$ curves intersect at $T_c = 170$ °C, above which infinitely thick epitaxial Ge(001) layers can be grown.

The inset in Fig. 3 is a plot of the ratio $\Delta h/h_2$ of the thickness of the defective epitaxial sublayer to the total epitaxial thickness as a function of the film growth temperature T_s. While Δh increases from $\simeq 900$ Å at $T_s = 95$ °C to 3100
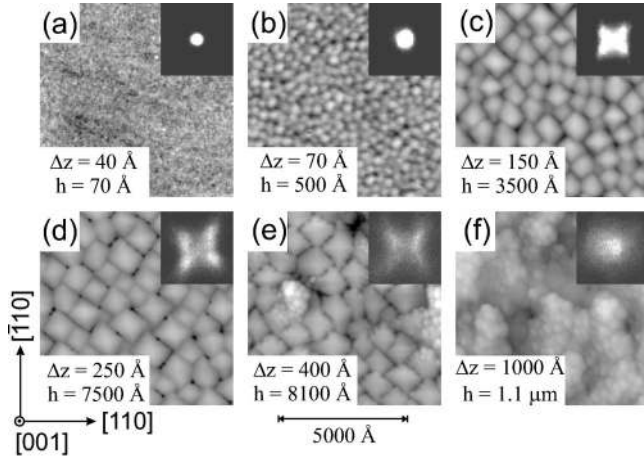
FIG. 4. AFM images of the surface of Ge(001) layers grown by LT-MBE at $T_s = 155$ °C with $R = 0.5$ Å s^{-1}. Film thicknesses h and black-to-white gray Δz scales are (a) $h = 70$ and $\Delta z = 40$ Å, (b) $h = 500$ and $\Delta z = 70$ Å, (c) $h = 3500$ and $\Delta z = 150$ Å, (d) $h = 7500$ and $\Delta z = 250$ Å, (e) $h = 8100$ and $\Delta z = 400$ Å, and (f) $h = 1.1$ μm and $\Delta z = 1000$ Å. The insets are two-dimensional slope histograms, ranging over $\pm 25°$ in the x and y directions, showing the directions of surface vector normals.

Å at 155 °C, $\Delta h / h_2$ continuously decreases from 0.81 at $T_s = 20$ °C to 0.29 at 155 °C to zero at $T_c \simeq 170$ °C. From Eq. (1), the temperature dependence of $\Delta h / h_2$ is

$$\frac{\Delta h}{h_2} \propto 1 - \exp\left[\frac{-(0.13 \text{ eV})}{kT_s} \right] \qquad (2)$$

corresponding to the solid line in the inset. $(E_1 - E_2) = 0.13$ eV is essentially equal to the previously reported free energy difference, 0.12 eV, between amorphous and crystalline Ge.[35,36]

AFM results were used to provide a quantitative measure of surface morphological evolution during Ge(001) LT-MBE as a function of T_s. Figures 4(a)–4(f) are typical AFM images and corresponding 2D slope histograms obtained from Ge layers deposited at $T_s = 155$ °C with thicknesses of 70 Å to 1.1 μm, corresponding to the RHEED patterns in Figs. 1(a)–1(f). Black-to-white gray scale values Δz were chosen to be four times the standard deviation of the height distribution around the average value and are therefore proportional to the surface width w. The surface of the 600-Å-thick Ge buffer layer (not shown) is essentially featureless and extremely flat with $w = 0.7$ Å.

During the initial stages of LT-MBE Ge(001) growth, the surface remains relatively flat, with a roughness, $w = 0.9$ Å, comparable to that of the buffer layer, as shown in Fig. 4(a) for a sample with $h = 70$ Å. Continued deposition results in the emergence of a regular arrangement of small, rounded mounds [Fig. 4(b), $h = 500$ Å] which coalesce with increasing layer thickness. w, d, and the aspect ratio w/d are plotted as a function of film thickness in Fig. 5. w increases continuously with h [Fig. 5(a)], ranging from 0.9 to 2.2 to 4.0 Å with $h = 70$, 500, and 1800 Å while d increases from 250 to 510 to 780 Å [Fig. 5(b)]. Both w and d can be fit over this
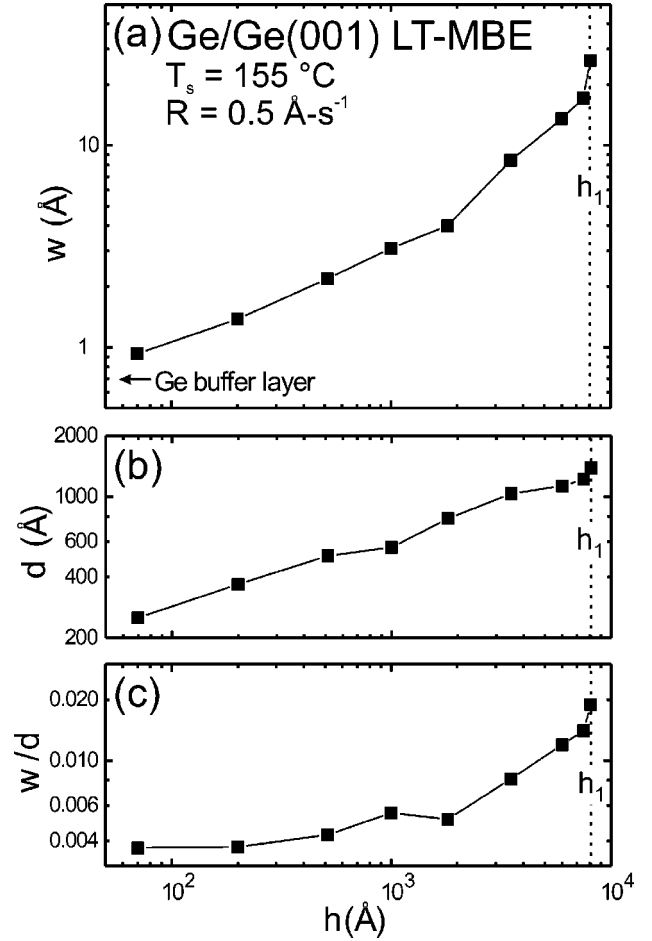

FIG. 5. (a) The surface width w, (b) in-plane coherence length d, and (c) the aspect ratio w/d as a function of film thickness for Ge(001) layers grown by LT-MBE at $T_s = 155$ °C with $R = 0.5$ Å s^{-1}.

thickness range using scaling relationships of the form $w \propto h^\beta$ and $d \propto h^n$. Physically, β is a measure of how fast surface roughness develops while n indicates the rate of island coarsening. Roughening and coarsening exponents are found to be $\beta \simeq 0.46$ and $n \simeq 0.35$, respectively, for $70 < h < 1800$ Å. Although the island vertical growth rate is larger than the in-plane expansion, the difference is relatively small. This leads, as shown in Fig. 5(c), to a slow increase in the aspect ratio w/d from $\simeq 0.0036$ to 0.0051 over this film thickness range. The intensity distributions in the two-dimensional (2D) slope histograms in the insets of Figs. 4(a) ($h = 70$ Å) and 4(b) ($h = 500$ Å) exhibit Gaussian shapes centered at the origin with no intensity beyond 2.4° and 3°, respectively, indicating that local surface slopes are extremely shallow.

The surface roughening rate changes discontinuously at $h \simeq 1800$ Å with β increasing from 0.46 to 1.08, while the mound coarsening rate remains approximately constant with $n \simeq 0.35$. Figure 5(a) shows that w increases from 4.0 Å at $h = 1800$ to 26.3 Å at $h = 8100$ Å as d increases from 780 to 1400 Å over the same film thickness range. Thus, the mound aspect ratio w/d, which exhibited a relatively slow increase with $h < 1800$ Å, rises rapidly at higher thicknesses, ranging

from 0.005 at $h = 1800$ Å to 0.019 at $h = 8100$ Å as the mounds grow much faster vertically than laterally.

Deposition to film thicknesses $h \gtrsim 1800$ Å also results in a transformation in surface mound shape from round to pyramidal structures composed of square bases with edges preferentially aligned along the elastically soft[37] $\langle 100 \rangle$ directions. The pyramidal islands coarsen and become better defined, with improved self-organization, as h increases. Typical images are presented in Figs. 4(c) and 4(d) for samples with thicknesses of 3500 and 7500 Å. At $h \gtrsim 7500$ Å deep cusps are observed, predominantly at island corners [see, for example, Fig. 4(d)]. Cusp formation occurs due to a combination of kinetic roughening, a consequence of low adatom mobilities and the presence of Ehrlich barriers at step edges, with atomic shadowing. Continued deposition results in wider and deeper trenches between adjoining islands together with more extensive cusps. The local onset of epitaxial breakdown is visible in AFM micrographs [e.g., Fig. 4(e), $h = 8100$ Å] at $h \gtrsim h_1(T_s)$ as clusters of small amorphous hillocks emerging from the cusps. The clusters were verified to be amorphous by XTEM selected area electron diffraction. With further deposition, the clusters grow vertically and laterally, eventually encompassing the entire surface of the film at $h \gtrsim h_2(T_s)$ as shown in Fig. 4(f).

Slope histograms for $T_s = 155$ °C layers with $h = 3500$ Å [inset in Fig. 4(c)] are characterized by intensity distributions which are within 4.2° of the [001] pole, compared to 3° for layers grown to $h = 500$ Å, with components which range out along the four $\langle 100 \rangle$ in-plane directions up to 5.2°. The latter indicates a tendency for facetting, consistent with the corresponding AFM image showing that the rounded growth mounds have transformed to pyramid-shaped structures. Facetting increases with increasing film thickness. At $h = 7500$ Å, most of the intensity in the slope histogram in Fig. 4(d) is contained in the lobes extending out to 7.5° along $\langle 100 \rangle$ and $\langle 010 \rangle$ directions. The marked decrease in intensity near the [001] pole indicates that the amount of flat surface area between trenches has greatly decreased. As the film thickness exceeds h_1, the 2D slope histograms become increasingly diffuse [see, for example, the insets in Figs. 4(e) and 4(f)] due to epitaxial breakdown with a corresponding loss in long-range surface order.

AFM measurements provide no topographical information near the bottom of the deeper cusps due to the finite tip size. In these regions, we use HR-XTEM to examine local surface morphology. Figures 6(a)–6(d) are typical [110] zone-axis bright-field HR-XTEM micrographs showing surface and near-surface features in Ge(001) LT-MBE layers grown at $T_s = 155$ °C. Figure 6(a) is an image of a single, relatively shallow, cusp in the surface of the $h = 7500$ Å Ge(001) layer of Fig. 4(d). The walls of the cusp form angles varying from 8° to 11° with respect to the film/substrate interfacial plane. Further deposition to $h = 8100$ Å leads to deeper cusps with a range of side wall angles from 20° to 55°. The cusp in Fig. 6(b) has a side wall angle of $\simeq 23 \pm 3°$. Figure 6(c) shows a different cusp in the same $h = 8100$ Å sample, this one bounded by {111} facet planes (side wall angle $= 54.7°$) forming the shape of an inverted pyramid. These cusps are associated with narrow ($\simeq 60$–75 Å) voided
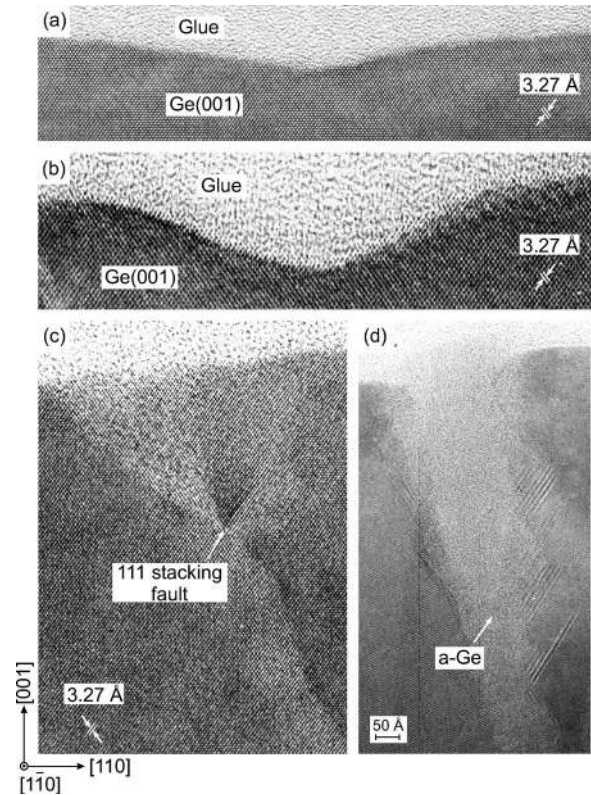

FIG. 6. High-resolution [110] bright-field XTEM micrographs of homoepitaxial Ge(001) layers grown by LT-MBE at $T_s = 155$ °C with $R = 0.5$ Å s^{-1} to thicknesses (a) $h = 7500$ Å and (b)–(d) $h = 8100$ Å.

regions which extend into the epitaxial sublayer at an angle of $\simeq 20°$ to the substrate normal. LT-MBE Ge(001) growth on {111} planes leads to the formation of 111 stacking faults [also shown in Fig. 6(c)] which are initiated by double-positioning defects. A lower-resolution XTEM image [Fig. 6(d)] of a different region of the same sample shows that the transition from epitaxial to amorphous Ge occurs along {111} facets.

In order to examine the surface morphology at the onset of epitaxial breakdown, Ge(001) layers were grown to thicknesses $h \simeq h_1(T_s)$. Typical examples are presented in Fig. 7 for films deposited at $T_s = 95$–165 °C. The surfaces of films grown to h_1 at $T_s \lesssim 115$ °C consist of mounds which are compact and round shaped. As T_s is increased from 95 to 115 °C, the mounds coarsen and exhibit improved alignment along $\langle 100 \rangle$ directions [compare, for example, Fig. 7(a) corresponding to $T_s = 95$ °C and $h_1 = 560$ Å with Fig. 7(b), $T_s = 110$ °C and $h_1 = 950$ Å]. At $T_s > 115$ °C ($h_1 = 1800$ Å), the surface features are transformed from round mounds to pyramidal islands with square bases [see Fig. 7(c)]. Deposition to $h = h_1$ at still higher T_s values leads to larger, primarily due to coalescence, and better-defined pyramid structures with enhanced self-organization along $\langle 100 \rangle$ directions. Deep cusps are more easily visible in layers deposited at higher T_s due to the larger lateral length scales. The images shown in Figs. 7(d)–7(f) correspond to growth temperatures ranging from 140 to 165 °C with $h_1 = 4350$ Å to 1.01 μm.
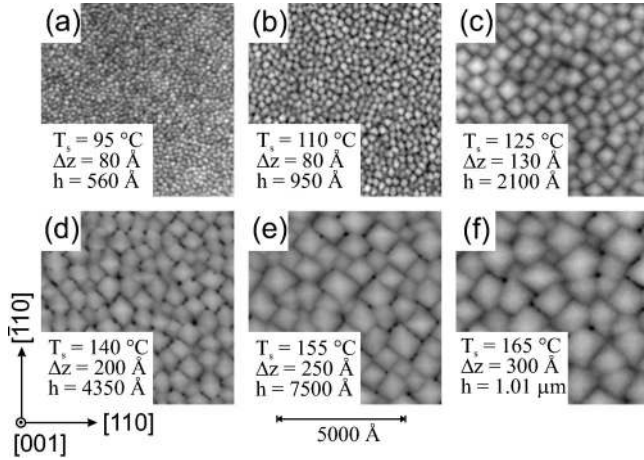
Figures 8(a)–8(c) are plots of w and w/h_1, d, and the

FIG. 7. AFM images of the surfaces of Ge(001) films grown by LT-MBE at temperatures T_s with $R = 0.5$ Å s^{-1} to critical epitaxial thicknesses $h_1(T_s)$. (a) $T_s = 95$ °C and $h = 560$ Å, (b) $T_s = 110$ °C and $h = 950$ Å, (c) $T_s = 125$ °C and $h = 2100$ Å, (d) $T_s = 140$ °C and $h = 4350$ Å, (e) $T_s = 155$ °C and $h = 7500$ Å, and (f) $T_s = 165$ °C and $h = 1.01$ μm. Δz is the black-to-white gray scale range.

aspect ratio w/d for Ge(001) layer thicknesses $h = h_1(T_s)$ as a function of T_s. Figure 8(a) shows that the surface width at the onset of defect formation is larger at higher film growth temperatures. $w(h_1)$ increases from 4.5 Å at $T_s = 95$ °C to 22.7 Å at 165 °C. However, as also shown in Fig. 8(a), the surface width w at $h_1(T_s)$ normalized to h_1 decreases from 6.9×10^{-3} at $T_s = 95$ °C to 2.2×10^{-3} at 165 °C.

The in-plane surface coherence length d at $h = h_1$ increases with T_s due to the corresponding increase in $h_1(T_s)$ which allows additional island coalescence. $d(h_1)$ varies from $\simeq 300$ Å at $T_s = 95$ °C to 1330 Å at 165 °C. A comparison of Figs. 8(a) and 8(b) reveals that the slopes of $w(h_1)$ and $d(h_1)$ vs T_s are essentially equal, thus the mound aspect ratio at h_1 [Fig. 8(c)] remains constant at $w/d \simeq 0.02$ irrespective of film growth temperature. This provides a direct correlation between kinetic surface roughening and the onset of epitaxial breakdown at h_1.

The adsorption of hydrogen during film deposition (H_2 is the primary background gas in all MBE systems) has been proposed as the primary mechanism limiting low-temperature epitaxy.[26,29,38] From Ref. 38, it is clear that H coverages $\gtrsim 1$ ML significantly increase the surface roughening rate and reduce LT-MBE Si(001) epitaxial thicknesses. This presumably occurs due to H atoms terminating surface dangling bonds[39] and inhibiting Si adatom diffusion.[40] We demonstrate below, however, that in the absence of significant H surface coverages, LT epitaxial breakdown of covalent semiconductors occurs as a result of a fundamental growth mode transition driven by kinetic roughening.

Due to the low reactive sticking probability of H_2 on Si(001),[41] even large H_2 partial pressures have no effect on $h_1(T_s)$ and $h_2(T_s)$ provided unshielded hot filaments and electron beams (we use a Knudsen cell to evaporate Ge) are switched off to avoid cracking the gas. We demonstrate this by repeating our LT-MBE Ge(001) growth experiments in H_2
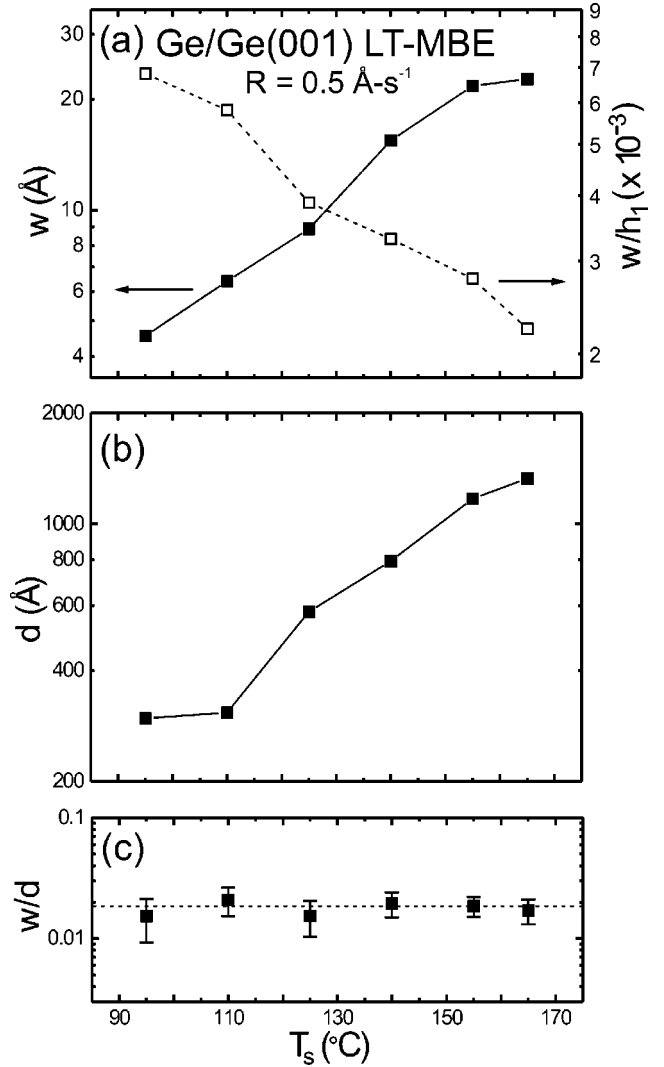

FIG. 8. (a) Surface width w and average roughening rate w/h_1, (b) in-plane length scale d, and (c) aspect ratio w/d as a function of substrate temperature T_s for Ge(001) layers grown by LT-MBE with $R = 0.5$ Å s^{-1} to critical epitaxial thicknesses $h_1(T_s)$.

partial pressures P_{H_2} of 1×10^{-8} and 1×10^{-7} Torr at $T_s = 110$ °C. We obtain identical results for h_1 and h_2, as well as for average mound widths and separations w and d at the critical thickness h_1. The surface morphology consists, in all cases, of compact rounded islands preferentially aligned along $\langle 100 \rangle$ directions as shown in Fig. 7(b).

IV. DISCUSSION

The results presented in Sec. III show that LT-MBE growth of homoepitaxial Ge(001)2×1 layers result in kinetic roughening which ultimately leads, for $T_s \lesssim 170$ °C, to epitaxial breakdown. Three distinct sublayers are obtained in this low-adatom-mobility 2D multilayer growth regime. The films are structurally perfect, as judged by high-resolution TEM/XTEM, up to a thickness $h_1(T_s)$. RHEED, AFM, and HR-XTEM results show that the surface morphology evolves via the formation of a periodic array of self-organized round

growth mounds which, for deposition at $T_s > 115\,°C$, transform to a pyramidal shape with square bases having edges aligned along $\langle 100 \rangle$ directions. Continuing film growth to thicknesses $h > h_1(T_s)$ leads to the formation of a defective, but still epitaxial, sublayer containing 111 stacking faults and microtwins. Deep cusps bounded by {111} facets form in interisland trenches at the corners of adjacent pyramids. At $h_2(T_s)$, there is an irreversible transition from defective epitaxy to amorphous deposition which is atomically abrupt locally but whose interface is globally quite rough.

AFM analyses show that from the earliest stages of LT-MBE, kinetic roughening gives rise to the formation of shallow round growth mounds which tend to self-organize along $\langle 100 \rangle$ directions. The surface width w and mean interisland separation d increase continuously with h as the surface roughens and the mounds coarsen following power laws of the form $w \propto h^\beta$ and $d \propto h^n$. The roughening exponent of Ge(001) layers grown at $T_s = 155\,°C$ is $\beta \simeq 0.46$ with $h \leqslant 1800\,\text{Å}$ and 1.08 for $1800\,\text{Å} < h \leqslant 8100\,\text{Å}$ while the coarsening rate remains constant at $n \simeq 0.35$ over the entire thickness range. Our results are in excellent agreement with the STM analyses of Van Nostrand *et al.*[4,7,42] which yield $\beta \simeq 1.0$ and $n \simeq 0.4$ at the same T_s. The sharp increase we observe in β with $h > 1800\,\text{Å}$ is attributed to a transformation in the surface features from round mounds to facetted pyramidal islands [compare, for example, Figs. 4(b) and 4(c)]. At constant film thickness, the surface roughness decreases with increasing T_s.

The onset of epitaxial breakdown during Ge(001) LT-MBE was investigated using quantitative AFM analyses of films grown to $h = h_1(T_s)$. The surface morphology of layers deposited to $h \simeq h_1$ at $T_s \lesssim 115\,°C$, is composed of small, $d \lesssim 300\,\text{Å}$, compact rounded mounds. A comparison of Figs. 7(a)–7(f) shows that Ge(001) deposition at higher T_s, giving rise to larger h_1 values, leads to additional island coalescence resulting in larger mounds and increased surface roughness at $h_1(T_s)$. The higher-temperature mounds also exhibit enhanced self-alignment along $\langle 100 \rangle$ rows. As T_s is increased above $115\,°C$ (corresponding to $h_1 = 1750\,\text{Å}$), the mounds at $h_1(T_s)$ transform to pyramidal-shaped islands with a square base [compare, for example, Figs. 7(a) and 7(b) with 7(c)–7(f)].

As h approaches h_1, the aspect ratio of the pyramidal surface islands increases rapidly (see Fig. 5) giving rise to deeper interisland trenches. The trenches result from incomplete filling, due to atomic shadowing, of lower pyramid terraces. Cusps bounded by {111} planes, the low-energy faces in the diamond crystal structure,[43,44] form at the base of the trenches, primarily in the corners of adjacent sets of pyramids. The {111} facets originate at corners since the pyramids have edges along $\langle 100 \rangle$ while the facets are constrained to lie along $\langle 110 \rangle$ directions. HR-XTEM micrographs (Fig. 6) also reveal that shallower corner cusps coexist with the {111} facets in samples with $h > h_1$. Higher-order {11*l*} facets, e.g., {113}, {115}, and {117} with side wall angles of 25.2°, 15.8°, and 11.4°, also lie along $\langle 110 \rangle$ directions. The cusp regions represent a small fraction of the total surface
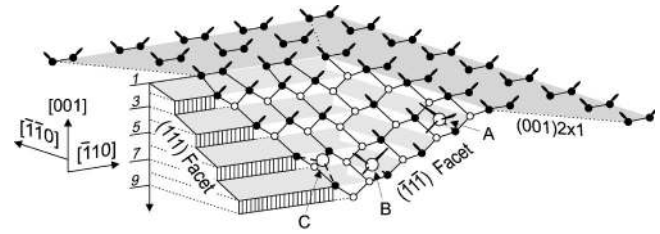

FIG. 9. Schematic drawing of an ideal surface cusp, bounded by {111} facets, which forms at the base of interisland trenches at the surface of LT-MBE Ge(001) layers prior to the onset of epitaxial breakdown. Adatom A is shown bonded in an epitaxial configuration on a $(\bar{1}1\bar{1})$ facet, B is a double-positioning defect, and adatom C is in a faulted $\sqrt{3} \times \sqrt{3}$ site on a (111) facet.

area and hence {111} facets are not visible in corresponding 2D slope histograms.

Growth beyond h_1 leads, through the combination of limited adatom mobility and atomic shadowing, to a reduction in the deposition rate at cusps. This results in incomplete coalescence of pyramids and the formation of columnar structures separated by intercolumnar voids [see, for example, Figs. 2(a)–2(c) and Fig. 6(c)]. The spacing between voided regions correlates with the mean interisland separation, $d = 1400\,\text{Å}$ for $T_s = 155\,°C$, at h_1. Note that the intercolumnar voids are oriented $\simeq 20°$ from the substrate normal and in the direction of the incident flux as shown, for example, in Fig. 6(c).

We find that LT-MBE Ge(001) films deposited on rotating substrates also exhibit extended voided structures with the same spacing, but with columns which are orthogonal to the substrate surface. Voided regions have also been observed during LT-MBE growth of Si(001) (Refs. 45 and 46) and are likely to be the origin of defects observed in LT-MBE Si(001) layers by post-deposition positron annihilation spectroscopy.[47,48] Homoepitaxial LT Si(001) films grown using hyperthermal beams[11,12] and ion-assisted deposition techniques[49] do not exhibit void formation due to collisionally induced enhanced adatom mobilities which serve to fill voids during island coalescence.

Low-temperature deposition on the {111} facets leads to the formation of a defective sublayer containing 111 stacking faults and microtwins, which we observe by RHEED and XTEM. Compared to {001} surfaces, {111} planes have higher atom densities, exhibit more complex reconstructions, and have a higher activation barrier to adatom diffusion.[15,50,51] Alternating {111} planes in the diamond crystal structure have 1 and 3 dangling bonds (db's), respectively. Figure 9 is a schematic illustration of a {111} faceted cusp terminated with individual atoms each having one db. Adatoms arriving on such surfaces can be accommodated at several possible sites, three of which are labeled A, B, and C in Fig. 9. Adatom A is pictured as bonding in an epitaxial configuration, with its db's aligned along the $[\bar{1}\bar{1}0]$ and $[110]$ directions, thus continuing the ABC stacking sequence of the (111) plane. There are, however, two symmetry-related configurations giving rise to double-positioning defects. One is shown by adatom B, which involves a 60° rotation about the bond axis leading to stacking faults. If the rotation cor-

responds to 180°, a 111 microtwin is formed (not shown). Adatom C reacts at a threefold $\sqrt{3} \times \sqrt{3}$ faulted hollow site which passivates three Db's while providing only one Db of its own.

Positioning of adatoms in sites such as B and C leads to a rapid loss of long-range order, resulting in the conversion to amorphous layer growth at $h = h_2(T_s)$. This growth-mode transition can be very abrupt as adatoms trapped at, for example, C sites completely alter the {111} surface-potential template. Small increases in adatom diffusivities on the {111} facets at higher T_s result in higher stacking fault densities since a faulted epitaxial layer is in a lower energy state than an amorphous layer.

As shown in Fig. 3, both critical epitaxial thicknesses h_1 and h_2 increase continuously with T_s, following Arrhenius relationships with activation energies of $E_1 \simeq 0.61$ and $E_2 \simeq 0.48$ eV. E_1 is approximately equal to the activation energy $E_m \simeq 0.65$ eV for the diffusion of Ge adatoms on the Ge(001)2×1 surface in directions parallel to the underlying dimer rows,[7] while $(E_1 - E_2)$ is essentially equal to the reported value for the enthalpy difference per atom, 0.12 eV, between amorphous and crystalline Ge.[35,36] Moreover, the thermal energy ($kT_s = 0.038$ eV) associated with the critical temperature $T_c \simeq 170$ °C is close to the best estimate of the Ehrlich barrier on Ge(001) surfaces $E_b \simeq 0.045$ eV.[4,7,42] When the deposition temperature exceeds T_c, the interisland trenches do not become deep enough to reach the critical aspect ratio, and, hence, the epitaxial thickness h_1 is infinite. Thus, interlayer mass transport plays a decisive role not only in determining surface roughening during multilayer growth, but also in controlling the extent of epitaxy.

Since cusp formation leading to the onset of epitaxial breakdown occurs when the surface roughness reaches a critical aspect ratio, irrespective of T_s, there must be a direct relationship between the critical layer thicknesses plotted in Fig. 3 and the adatom surface diffusivity. If we mechanistically define the onset of epitaxial breakdown as the film thickness at which w and d become sufficiently large that the island peak to valley distance x is greater than the adatom mean diffusion length L, we can estimate the T_s dependence of h_1. That is, cusps form when $x \gtrsim L$ because adatoms cannot fill the trenches during deposition. Since the island side walls form angles which are very shallow (aspect ratio $\lesssim 0.02$), x can be approximated as half the mean interisland separation d through the expression

$$x \simeq \frac{d}{2} = \frac{Bh^n}{2}, \qquad (3)$$

where h is the layer thickness, B is a constant, and n is the coarsening exponent. From universal scaling theory[52] and experimental observations[53–56] during film growth, L is related to the surface diffusivity D, and the deposition rate R through the expression

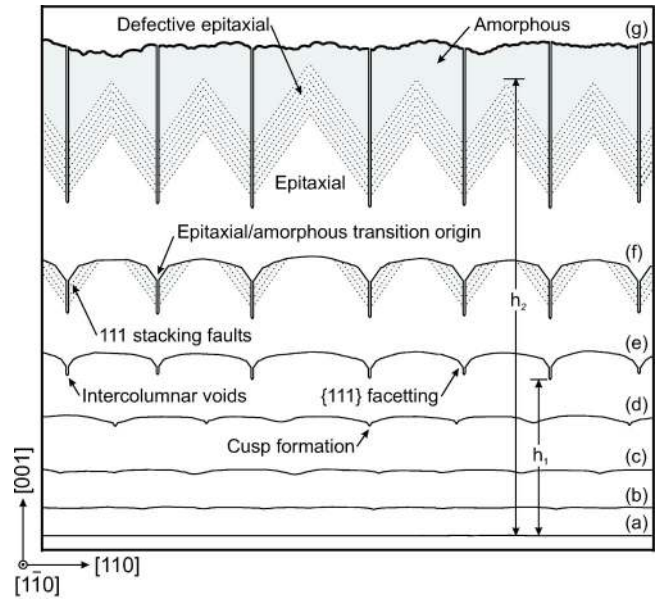$$L \propto \left(\frac{D_s}{R} \right)^\alpha, \qquad (4)$$

FIG. 10. Schematic diagram illustrating the time (i.e., film thickness) microstructural and surface morphological evolution during LT-MBE growth of Ge(001).

where $D_s = D_0 \exp(-E_m/kT_s)$ and the exponent α depends upon the critical nucleus size and ranges from $\frac{1}{6}$ to $\frac{1}{2}$. Setting $x = L$ yields an expression for h_1 as a function of T_s,

$$h_1 = \left[\frac{2}{B} \left(\frac{D_0}{R} \right)^\alpha \right]^{1/n} \exp\left(\frac{-E_m \alpha}{nkT_s} \right). \qquad (5)$$

In our experiments, $R = 0.5$ Å s^{-1}, $E_m = 0.65$ eV, and $n \simeq 0.35$. The preexponential factor D_0 is determined from the expression $D_0 = (b^2 \nu/4)$ in which $b = 4$ Å is the surface lattice constant along dimer rows and $\nu = 8.27 \times 10^{12}$ s^{-1} is the Ge Debye frequency.[57] The best fit to $h_1(T_s)$, as shown by the solid line in Fig. 3, is obtained with $\alpha = \frac{1}{3}$ and $B = 11.22$.

The above experimental results and analyses can be assembled to develop an atomistic growth model describing epitaxial breakdown. A schematic two-dimensional cross-sectional view of the evolving Ge(001) surface with increasing h is shown in Fig. 10. During the early stages of film growth, the surface is very smooth, with a roughness comparable to that of the buffer layer [Fig. 10(a)]. Low adatom mobilities combined with Ehrlich barriers, and/or deep traps at step edges, to the migration of adatoms over down-steps lead to a divergence in adatom flux and, hence, increased nucleation on terraces. As growth continues and the multilevel islands coalesce, trenches are formed between the islands as illustrated in Figs. 10(b) and 10(c). The trenches become deeper and wider, i.e., the amplitude of the roughness increases, as deposition proceeds in the 2D multilayer growth regime. Incomplete filling of terraces leads to the development of deep cusps bounded by {11l} facets [Fig. 10(d)] which eventually transform into low-energy {111} surfaces [Fig. 10(e)]. Atomic shadowing in the cusps results in incomplete island coalesce and the subsequent formation of intercolumnar voids.

The transition from epitaxial to amorphous growth is initiated on {111} facetted cusps, where 111 stacking faults form due to double-positioning defects, as described above. The stacking faults quickly progress vertically and laterally along {111} facet planes as illustrated in Fig. 10(f). The growth mode initially transforms from crystalline to amorphous in the cusps, with the regions between adjacent valleys still epitaxial. The large-scale lateral epitaxial/amorphous interface, as shown in the XTEM images in Fig. 2, forms when 111 stacking faults at cusps on opposite corners or sides of individual islands meet and hence completely transform the film to an amorphous overlayer at a thickness h_2 as shown in Fig. 10(g). The size of the 2D projections increases with increasing T_s since the separation between individual mounds and hence cusps at h_1 is larger. Intercolumnar voids continue through the defective epitaxial sublayer into the amorphous region, creating a columnar microstructure.

V. CONCLUSION

Epitaxial breakdown of Ge(001) layers grown by LT-MBE at $R = 0.5$ Å s^{-1} over the temperature range $T_s = 95$–190 °C was investigated. Growth below a critical temperature $T_c \simeq 170$ °C results in limited epitaxial thicknesses and the emergence of three distinct sublayers. The first region is defect free and fully epitaxial, extending to a thickness h_1. Kinetic roughening during growth to thicknesses $h \lesssim h_1$ results in monotonic, T_s-dependent increases in the surface width w and mean interisland separation d. Surface morphology evolves via the formation of a periodic array of self-organized round growth mounds which, for deposition at $T_s > 115$ °C, transform to a pyramidal shape with square bases having edges aligned along $\langle 100 \rangle$ directions. Epitaxial breakdown at h_1 occurs as the surface roughness reaches a critical T_s-independent aspect ratio $w/d \simeq 0.02$. The combination of low adatom mobilities and the presence of step-edge Ehrlich barriers results in the formation of {111} faceted cusps at interisland trenches. Atomic shadowing in the cusps gives rise, in turn, to the formation of intercolumnar voids. Adatom double-positioning and other symmetry-related defects on the {111} facets then lead to the formation of stacking faults, microtwins, and an irreversible transformation to amorphous overlayer growth at a critical film thickness h_2. $h_1(T_s)$ and $h_2(T_s)$ follow relationships $h_{1(2)} \propto \exp(-E_{1(2)}/kT_s)$, where E_1 is 0.61 eV and $E_2 = 0.48$ eV. E_1 is approximately equal to the Ge adatom diffusion barrier on Ge(001). Both $h_1(T_s)$ and $h_2(T_s)$ are unaffected by the presence of H$_2$ background gas, even at partial pressures up to 10^{-7} Torr. Thus, low-temperature epitaxial breakdown during our Ge(001) MBE growth experiments is a growth-mode transition and we have conclusively demonstrated that there is a direct correlation between epitaxial breakdown at $w/d \simeq 0.02$ and kinetic roughening.

*Also at: Département de génie physique, École Polytechnique de Montréal, C.P. 6079, Succ. Centre-Ville, Montréal, Québec H3C 3A7 Canada.

[1] J. Villain, J. Phys. I **1**, 19 (1991).

[2] J. Lapujoulade, Surf. Sci. Rep. **20**, 191 (1994).

[3] M. D. Johnson, C. Orme, A. W. Hunt, D. Graff, J. Sudijono, L. M. Sander, and B. G. Orr, Phys. Rev. Lett. **72**, 116 (1994).

[4] J. E. Van Nostrand, S. J. Chey, M.-A. Hasan, D. G. Cahill, and J. E. Greene, Phys. Rev. Lett. **74**, 1127 (1995).

[5] J. A. Stroscio, D. T. Pierce, M. D. Stiles, A. Zangwill, and L. M. Sander, Phys. Rev. Lett. **75**, 4246 (1995).

[6] N.-E. Lee, D. Cahill, and J. E. Greene, Phys. Rev. B **53**, 7876 (1996).

[7] J. E. Van Nostrand, S. J. Chey, and D. G. Cahill, Phys. Rev. B **57**, 12 536 (1998).

[8] B. W. Karr, I. Petrov, P. Desjardins, D. G. Cahill, and J. E. Greene, Surf. Coat. Technol. **94-95**, 12 536 (1998).

[9] C. Schelling, G. Springholz, and F. Schaffler, Thin Solid Films **369**, 1 (2000).

[10] G. Ehrlich and F. G. Hudda, J. Chem. Phys. **44**, 1039 (1966); S. C. Wang and G. Ehrlich, Phys. Rev. Lett. **70**, 41 (1993); **71**, 4174 (1993); G. Ehrlich, Surf. Sci. **331/333**, 865 (1995); A. Gölzhäuser and G. Ehrlich, Phys. Rev. Lett. **77**, 1334 (1996).

[11] N.-E. Lee, G. A. Tomasch, and J. E. Greene, Appl. Phys. Lett. **65**, 3236 (1994).

[12] N.-E. Lee, G. Xue, and J. E. Greene, J. Appl. Phys. **80**, 769 (1996).

[13] G. Xue, H. Z. Xiao, M.-A. Hasan, J. E. Greene, and H. K. Birnbaum, J. Appl. Phys. **74**, 2512 (1993).

[14] F. Jona, Appl. Phys. Lett. **9**, 235 (1966).

[15] T. de Jong, W. A. S. Douma, L. Smit, V. V. Koablev, and F. W. Saris, J. Vac. Sci. Technol. B **1**, 888 (1983).

[16] J. Aarts, W. M. Gerits, and P. K. Larsen, Appl. Phys. Lett. **48**, 931 (1986).

[17] H. Jorke, H.-J. Herzog, and H. Kibbel, Phys. Rev. B **40**, 2005 (1989); H. Jorke, H. Kibbel, F. Schaffler, and H.-J. Herzog, Thin Solid Films **183**, 309 (1989).

[18] D. J. Eaglesham, H.-J. Gossman, and M. Cerullo, Phys. Rev. Lett. **65**, 1227 (1990).

[19] D. J. Eaglesham, H.-J. Gossman, M. Cerullo, L. N. Pfeiffer, and K. C. West, J. Cryst. Growth **111**, 833 (1991).

[20] O. P. Karpenko, S. M. Yalisove, and D. J. Eaglesham, J. Appl. Phys. **82**, 1157 (1997).

[21] D. J. Eaglesham, L. N. Pfeiffer, K. W. West, and D. R. Dykaar, Appl. Phys. Lett. **58**, 65 (1991).

[22] D. J. Eaglesham and M. Cerullo, Appl. Phys. Lett. **58**, 2276 (1991).

[23] O. Gurdal, P. Desjardins, J. R. A. Carlsson, N. Taylor, H. H. Radamson, J.-E. Sundgren, and J. E. Greene, J. Appl. Phys. **83**, 162 (1998).

[24] P. Desjardins, T. Spila, O. Gürdal, N. Taylor, and J. E. Greene, Phys. Rev. B **60**, 15 993 (1999).

[25] D. J. Eaglesham, J. Appl. Phys. **77**, 3597 (1995).

[26] S. H. Wolff, S. Wagner, J. C. Bean, R. Hull, and J. M. Gibson, Appl. Phys. Lett. **55**, 2017 (1989).

[27] D. P. Adams, S. M. Yalisove, and D. J. Eaglesham, Appl. Phys. Lett. **63**, 3571 (1993).

[28] D. J. Eaglesham, F. C. Unterwald, H. Luftman, D. P. Adams, and S. M. Yalisove, J. Appl. Phys. **74**, 6615 (1993).

[29] P. Asoka-Kumar, S. Szpala, B. Nielsen, Cs. Szeles, K. G. Lynn, W. A. Lanford, C. A. Shepard, and H.-J. Gossman, Phys. Rev. B **51**, 4630 (1995).

[30] J. Thiesen, H. M. Branz, and R. S. Crandall, Appl. Phys. Lett. **77**, 3589 (2000).

[31] X.-J. Zhang, G. Xue, A. Agarwal, R. Tsu, M.-A. Hasan, J. E. Greene, and A. Rockett, J. Vac. Sci. Technol. A **11**, 2553 (1993).

[32] M. G. Lagally, in *Methods of Experimental Physics*, edited by R. L. Park and M. G. Lagally (Academic, New York, 1985), Vol. 22.

[33] M. Henzler, in *Electron Spectroscopy for Surface Analysis*, edited by H. Ibach, Vol. 4 of *Topics in Current Physics* (Springer, Berlin, 1977).

[34] C. Argile and G. E. Rhead, Surf. Sci. Rep. **10**, 227 (1989).

[35] P. Germain, K. Zellama, S. Squelard, J. C. Bourgoin, and A. Gheorghiu, J. Appl. Phys. **50**, 6986 (1979).

[36] E. P. Donovan, F. Spaepen, D. Turnbull, J. M. Poate, and D. C. Jacobson, J. Appl. Phys. **57**, 1795 (1985).

[37] V. A. Shchukin, N. N. Ledentsov, P. S. Kop'eV, and D. Bimberg, Phys. Rev. Lett. **75**, 2968 (1995).

[38] M. Copel and R. M. Tromp, Phys. Rev. Lett. **72**, 1236 (1994).

[39] T. R. Bramblett, Q. Lu, T. Karasawa, M.-A. Hasan, S. K. Jo, and J. E. Greene, J. Appl. Phys. **76**, 1884 (1994).

[40] J. E. Vasek, Z. Zhang, C. T. Sallling, and M. G. Lagally, Phys. Rev. B **51**, 17 207 (1995).

[41] K. W. Kolasinski, W. Nessler, K.-H. Bornsceuer, and E. Hasselbrink, J. Chem. Phys. **1010**, 7082 (1994).

[42] J. E. Van Nostrand, Ph.D. thesis, University of Illinois at Urbana-Champaign, 1996.

[43] D. J. Eaglesham, A. E. White, L. C. Feldman, N. Moriya, and D. C. Jacobson, Phys. Rev. Lett. **70**, 1643 (1993).

[44] D. M. Follstaedt, Appl. Phys. Lett. **62**, 1116 (1993).

[45] D. D. Perovic, G. C. Weatherly, P. J. Simpson, P. J. Schultz, T. E. Jackman, G. C. Aers, J.-P. Noël, and D. C. Houghton, Phys. Rev. B **43**, 14 257 (1991).

[46] D. D. Perovic, G. C. Weatherly, J.-P. Noël, and D. C. Houghton, J. Vac. Sci. Technol. B **9**, 2034 (1991).

[47] H.-J. Gossman, P. Asoka-Kumar, T. C. Leung, B. Nielsen, K. G. Lynn, F. C. Unterwald, and L. C. Feldman, Appl. Phys. Lett. **61**, 540 (1992).

[48] Cs. Szeles, P. Asoka-Kumar, K. G. Lynn, H.-J. Gossman, F. C. Unterwald, and T. Boone, Appl. Phys. Lett. **66**, 2855 (1995).

[49] D. L. Smith, C.-C. Chen, G. B. Anderson, and S. B. Hagstrom, Appl. Phys. Lett. **62**, 570 (1993).

[50] See, for example, *Si Molecular Beam Epitaxy*, edited by E. Kasper and J. C. Bean (CRC, Boca Raton, FL, 1988), and articles referenced therein.

[51] H.-J. Gossmann and L. C. Feldman, Phys. Rev. B **32**, 6 (1985).

[52] A. Pimpinelli and J. Villain, *Physics of Crystal Growth* (Cambridge University Press, Cambridge, U.K., 1998), p. 181.

[53] Y. W. Mo, J. Kleiner, M. B. Webb, and M. G. Lagally, Surf. Sci. **268**, 275 (1992).

[54] J. A. Stroscio, D. T. Pierce, and R. A. Dragoset, Phys. Rev. Lett. **70**, 3615 (1993).

[55] J.-P. Bucher, E. Hahn, P. Fernandez, C. Massobrio, and K. Kern, Europhys. Lett. **27**, 473 (1994).

[56] I. K. Robinson, K. L. Whiteaker, and D. A. Walko, Physica B **221**, 70 (1996).

[57] $\theta_D = 375$ K for Ge (Ref. 2) and $\nu = k\theta_D/h$ where k and h are Boltzmann's and Planck's constants, respectively.